

Density functional study of oxygen on Cu(100) and Cu(110) surfaces

X. Duan,^{1,*} O. Warschkow,^{1,†} A. Soon,¹ B. Delley,² and C. Stampfl¹

¹*School of Physics, The University of Sydney, Sydney, New South Wales 2006, Australia*

²*Paul-Scherrer-Institut, WHGA/123, Villigen CH-5232, Switzerland*

(Received 20 July 2009; revised manuscript received 11 November 2009; published 23 February 2010)

Using density-functional theory within the generalized gradient approximation, we investigate the interaction between atomic oxygen and Cu(100) and Cu(110) surfaces. We consider the adsorption of oxygen at various on-surface and subsurface sites of Cu(100) for coverages of 1/8 to 1 monolayers (ML). We find that oxygen at a coverage of 1/2 ML preferably binds to Cu(100) in a missing-row surface reconstruction, while oxygen adsorption on the nonreconstructed surface is preferred at 1/4 ML coverage consistent with experimental results. For Cu(110), we consider oxygen binding to both nonreconstructed and added-row reconstructions at various coverages. For coverages up to 1/2 ML coverage, the most stable configuration is predicted to be a $p(2 \times 1)$ missing-row structure. At higher oxygen exposures, a surface transition to a $c(6 \times 2)$ added strand configuration with 2/3 ML oxygen coverage occurs. Through surface Gibbs free energies, taking into account temperature and oxygen partial pressure, we construct (p, T) surface phase diagrams for O/Cu(100) and O/Cu(110). On both crystal faces, oxygenated surface structures are stable prior to bulk oxidation. We combine our results with equivalent (p, T) surface free energy data for the O/Cu(111) surface to predict the morphology of copper nanoparticles in an oxygen environment.

DOI: [10.1103/PhysRevB.81.075430](https://doi.org/10.1103/PhysRevB.81.075430)

PACS number(s): 68.43.Bc, 81.65.Mq, 68.47.Gh

I. INTRODUCTION

Copper-based catalysts are of importance to a number of industrial processes including the synthesis of methanol,¹ the reduction and decomposition of nitrogen oxides,^{2–4} the oxydehydrogenation of ammonia,^{5,6} electroless plating,⁷ fuel cell electrodes,⁸ and the treatment of waste water.⁹ In copper catalysis—as for many other metal catalysts—surface oxidation and oxidic overlayers are widely believed to play a crucial role.^{10,11}

Oxygen adsorption on Cu(100) has been the subject of numerous studies^{12–36} and a number of distinct oxide reconstructions are known. Low energy electron diffraction (LEED) experiments^{14,19} identified a $(2\sqrt{2} \times \sqrt{2})R45^\circ$ reconstruction that appears at oxygen coverages above 0.3 ML. This phase is also observed in scanning tunneling microscopy (STM) and x-ray diffraction (XRD) experiments and was characterized as a missing-row (MR) reconstruction with an oxygen content of 1/2 ML.^{16,17,20,23} At low coverage (<0.3 ML), STM images show islands with a $c(2 \times 2)$ structure on the clean Cu(100) surface,²³ supporting earlier LEED evidence for the existence of such a reconstruction.¹⁹ Early theoretical work has rationalized the structural properties of the O/Cu(100) system in terms of orbital hybridization¹⁵ and charge transfer processes.¹⁸ More recent *ab initio* studies^{25–27} have focused on the two observed phases and discuss their formation in terms of the electronic structure. Kangas and co-workers,^{29,35} contrast the stability of oxygen at surface and subsurface sites for coverages up to 2 ML, finding stable subsurface binding at coverages above approximately 3/4 ML. Using density-functional theory and density-functional perturbation theory, Bonini *et al.*³¹ compare the $(2\sqrt{2} \times \sqrt{2})R45^\circ$ missing-row reconstructions of O/Cu(100) and O/Ag(100) and find similar structural and vibrational properties. An important insight was recently provided by the joint experimental and theoretical work of Iddir and

co-workers,³³ explaining the observed $(2\sqrt{2} \times \sqrt{2})R45^\circ$ and $c(2 \times 2)$ phases as two sides of an entropy-driven order-disorder transition.

On Cu(110), oxygen adsorption results in a major reconstruction of the surface.²⁰ Two well-ordered superstructures are known: a (2×1) phase with an oxygen coverage of 1/2 ML and a $c(6 \times 2)$ phase with a coverage of 2/3 ML. The oxygen-induced (2×1) reconstruction has been the subject of several experimental and theoretical studies,^{15,20,22,37–49} and the added row structure⁴¹ is now generally accepted. The oxygen-induced $c(6 \times 2)$ reconstruction is receiving increasing attention^{50–54} for its hypothesized role as a precursor phase of bulk oxidation. The transition between the (2×1) and $c(6 \times 2)$ surface phases was directly examined by Sun *et al.*⁵³ using reflectance difference spectroscopy which determined a transition temperature of 660 K.

In light of the importance of temperature and the availability of oxygen on determining surface reconstruction, we use the theoretical framework of *ab initio* atomistic thermodynamics^{11,55,56} to describe the relative stability of various O/Cu(100) and O/Cu(110) reconstructions in contact with a realistic gaseous environment. This leads us to a complete thermodynamic model of the stable surface phase between the oxygen-free surface to the bulk oxide Cu₂O. Importantly, the thermodynamical analysis shows that bulk Cu₂O formation imposes an upper limit on the oxygen coverage of the surface, which, interestingly, is very nearly the same for the three principal low-index surfaces (100), (110), and (111). The results presented here follow on, and complement, our earlier results for the O/Cu(111) surface.⁵⁷ This completes our free energy treatment of the three principal low-index surfaces of the oxygen-on-copper system at a consistent level of theory allowing free-energy comparisons between the three crystal phases. We use the combined free energy data to predict the morphology of copper nanoparticles in an oxygen environment.

Our discussion is organized as follows: In Sec. II, our computational methodology is detailed, including the definitions of several calculated quantities and a brief description of the *ab initio* atomistic thermodynamics approach. Section III A revisits the clean Cu(100) and Cu(110) surfaces, which serves to validate our methodology against previous results in the literature. In Sec. III B, we present our calculations for the O/Cu(100) system discussing energetic, structural, and electronic properties. The corresponding results for O/Cu(110) are presented in Sec. III C. In Sec. IV we combine our data into thermodynamic (p, T)-phase diagrams to facilitate comparison with experiment.

II. COMPUTATIONAL METHOD

All calculations are performed using density-functional theory (DFT) in the generalized gradient approximation (GGA; Perdew, Burke, and Ernzerhof exchange-correlation)⁵⁸ as implemented in the DMol³ software.⁵⁹ The electronic eigenfunctions are expanded in terms of a localized atomic orbital basis set of double numerical plus polarization (DNP) quality and a real-space cutoff of 9 Bohr. Our calculations include scalar-relativistic corrections. A thermal broadening of 0.1 eV is applied to improve the convergence of the self-consistent procedure.

For bulk copper, we use a $12 \times 12 \times 12$ Monkhorst-Pack grid to integrate over the Brillouin zone of the elemental fcc-unit cell and obtain a calculated lattice constant of 3.64 Å, in good agreement with experiment (3.61 Å).⁶⁰ The calculated bulk modulus and cohesive energy are 136 GPa and 3.45 eV, respectively; also in good agreement with the experimental values of 137 GPa and 3.49 eV.⁶⁰

Periodic slabs are used to model the surfaces of copper. The Cu(100) slab is composed of 9 atomic layers with an approximate thickness of 14.6 Å. The Cu(110) surface is represented using a slab of 11 atomic layers which is approximately 13.0 Å thick. Successive slabs in the three-dimensionally repeated unit cell are separated by a large vacuum region of ≈ 30 Å. In all our calculations, oxygen atoms are adsorbed on both surfaces of the slab in order to preserve inversion symmetry. In our geometry optimizations, three atomic layers at the center of the slab are held fixed at the calculated bulk positions. All other atoms are fully relaxed until all force components acting on the atoms are below 0.015 eV/Å. Test calculations using larger slabs have confirmed that the resultant error to the average oxygen binding energy and the Gibbs free surface energy (see definitions below) are smaller than 0.01 eV and 0.001 eV/Å², respectively.

Several surface supercells are used to study the effects of oxygen coverage, Θ , on the electronic and geometric structure of the surface. For the Cu(100) surface we consider coverages of between 1/8 and 1 ML, using (1×1) , (2×2) , (4×4) , $(2\sqrt{2} \times \sqrt{2})R45^\circ$, $(2\sqrt{2} \times 2\sqrt{2})R45^\circ$, and $c(4 \times 6)$ surface unit cells. For the large $c(4 \times 6)$ unit cell, computational restrictions necessitated a thinner, five-layer slab, as opposed to the regular nine-layer slab. This increases for this structure the error in the average oxygen binding energy and the Gibbs free surface energy to smaller than 0.03 eV and

0.002 eV/Å², respectively. For Cu(110), coverages of between 1/8 to 1 ML are achieved using (2×1) , (3×1) , (4×1) , (2×2) , (3×2) , (8×1) , (2×4) , and $c(6 \times 2)$ cells. Brillouin-zone integrations are performed using $(12 \times 12 \times 1)$ and $(6 \times 12 \times 1)$ Monkhorst-Pack grids for the (1×1) surface unit cells of Cu(100) and Cu(110), respectively. For the larger surface unit cells, correspondingly smaller grids are used to ensure an equivalent sampling of reciprocal space. The convergence with respect to \mathbf{k} -point density of binding energies and free surface energies to below 0.01 eV and 0.001 eV/Å², respectively, was earlier established by Soon *et al.*⁶¹ using the same computational model of the Cu surface.

Average binding energies per oxygen atom, E_b^O , are given relative to the clean surface and an isolated oxygen molecule. We calculate E_b^O as

$$E_b^O = -\frac{1}{N_O} \left(E_{O/Cu}^{\text{slab}} - E_{Cu}^{\text{slab}} - \Delta N_{Cu} E_{Cu} - \frac{N_O}{2} E_{O_2} \right), \quad (1)$$

where N_O is the number of adsorbed oxygen atoms, $E_{O/Cu}^{\text{slab}}$ is the total energy of the adsorbate-substrate system, E_{O_2} is the energy of an isolated oxygen molecule (see below), and E_{Cu}^{slab} is the energy of the clean surface. ΔN_{Cu} is the difference in the number of Cu atoms between the O/Cu system and the clean surface slab, and E_{Cu} is the energy of a Cu atom in bulk Cu. The term $\Delta N_{Cu} E_{Cu}$ accounts for differences in the number of Cu atoms, when we compare oxygen adsorption between clean, missing-row, and added-row reconstructions. Average binding energies are defined such that a positive value indicates a thermodynamically favorable adsorption process.

The energies of an oxygen molecule (E_{O_2}) and an isolated oxygen atom are obtained from spin-polarized calculations where we use a real-space basis set cutoff of 20 Bohr. Using these two energies, we calculate the molecular binding energy of an oxygen molecule to be 6.08 eV (or 3.04 eV per atom), somewhat larger than the experimental value of 5.12 eV (or 2.56 eV per atom). Our overestimation of the O₂ binding energy is inline with previous studies that use DFT in the GGA approximation.^{47,62} For the molecular bond length and the vibrational frequency we obtain 1.22 Å and 1544 cm⁻¹, respectively, in good agreement with the experimental values of 1.21 Å and 1580 cm⁻¹ (Ref. 63).

The effect of the gaseous environment on the relative stability of the considered surface structures is captured by the method of *ab initio* atomistic thermodynamics.^{11,55,56} The availability of oxygen from the environment is represented by the oxygen chemical potential, μ_O , which is a function of the gas-phase temperature and the oxygen partial pressure, p_{O_2} . For a given $\mu_O(p_{O_2}, T)$, the thermodynamically preferred surface is the one with the lowest Gibbs free energy γ which we calculate as

$$\Delta \gamma = \frac{1}{2A} (G_{O/Cu}^{\text{slab}} - G_{Cu}^{\text{slab}} - \Delta N_{Cu} \mu_{Cu} - N_O \mu_O). \quad (2)$$

In this equation, $\Delta \gamma$ is the surface Gibbs free energy relative to the oxygen-free, nonreconstructed surface. The calculated Gibbs free energies of the oxygenated and the oxygen-

free slab model used to represent the surface are denoted, $G_{\text{O/Cu}}^{\text{slab}}$ and $G_{\text{Cu}}^{\text{slab}}$, respectively. The term $\Delta N_{\text{Cu}}\mu_{\text{Cu}}$ represents the cost of exchanging Cu atoms with a reservoir with chemical potential μ_{Cu} . In our case, this reservoir is bulk copper with which the surface is assumed to be in equilibrium; thus, μ_{Cu} equals the free energy of a copper atom in bulk. In Eq. (2), the factor $\frac{1}{2A}$ is the reciprocal of the total (in-plane) surface area of the slab model (i.e., the sum of both sides). The factor serves to normalize to a common unit area the surface free energies of slabs of varying unit cells.

In our calculations, we neglect in $G_{\text{O/Cu}}^{\text{slab}}$ and $G_{\text{Cu}}^{\text{slab}}$ the free energy contributions due to vibrational motion and the pressure-volume term.⁵⁶ This allows us to replace these terms with the respective DFT total energies, $E_{\text{O/Cu}}^{\text{slab}}$ and $E_{\text{Cu}}^{\text{slab}}$. It is convenient to combine Eqs. (1) and (2) to obtain the surface free energy in terms of the average oxygen binding energy, i.e.,

$$\Delta\gamma \approx \frac{1}{2A}(-N_{\text{O}}E_b^{\text{O}} - N_{\text{O}}\Delta\mu_{\text{O}}), \quad (3)$$

In this equation, $\Delta\mu_{\text{O}}$ denotes the chemical potential given relative to the dissociation energy E_{O_2} of an isolated O_2 molecule, i.e., we define

$$\Delta\mu_{\text{O}} = \mu_{\text{O}} - \frac{1}{2}E_{\text{O}_2}. \quad (4)$$

In our electronic structure analysis, we consider electron density differences

$$n^{\Delta}(\mathbf{r}) = n^{\text{O/Cu}}(\mathbf{r}) - n^{\text{Cu}}(\mathbf{r}) - n^{\text{O}}(\mathbf{r}), \quad (5)$$

where $n^{\text{O/Cu}}(\mathbf{r})$ is the total electron density of the substrate-adsorbate system, and $n^{\text{Cu}}(\mathbf{r})$ and $n^{\text{O}}(\mathbf{r})$ are the electron densities of the clean substrate and the isolated O ad-layer, respectively. The density difference is evaluated and plotted for the relaxed adsorbate system, which highlights those regions near the surface where oxygen adsorption induces a depletion or accumulation of the electron density.

The surface dipole moment (in Debye) is evaluated using the Helmholtz equation

$$\mu = \frac{A\Delta\Phi}{12\pi\Theta}, \quad (6)$$

where A is the area (in \AA^2) of a (1×1) surface unit, and $\Delta\Phi$ is the work-function change (in eV) relative to the clean surface. The work function is defined as the difference between the electrostatic potential (U) in the middle of the vacuum region and the Fermi energy (E_F), so that,

$$\Delta\Phi = U - E_F - \Phi_{\text{clean}}, \quad (7)$$

where Φ_{clean} is the work function of the clean surface.

III. RESULTS

A. Clean Cu(100) and Cu(110) surfaces

The clean Cu(100) and Cu(110) surfaces are well characterized experimentally and theoretically in the literature.^{64–70} As a point of reference, we relax the atomic positions for

both surfaces and compare our calculated interlayer spacings with previously reported values. In the following, interlayer separations near the surface are given as percent changes Δ_{ij} relative to the respective bulk separations of 1.82 and 1.30 \AA in the $\langle 100 \rangle$ and $\langle 110 \rangle$ directions. For the Cu(100) surface, the change between the first and second atomic layer (this is denoted Δ_{12}) is calculated to be -2.3% , corresponding to a small contraction relative to bulk. Between the second and third layer the change is $\Delta_{23} = +1.0\%$. These values are in good agreement with previous DFT-GGA calculations⁶⁵ that report $\Delta_{12} = -2.6\%$ and $\Delta_{23} = +0.9\%$ and experimental LEED data^{68,69} with $\Delta_{12} = -2.1\%$ and $\Delta_{23} = +0.5\%$. For the Cu(110) surface, we obtain $\Delta_{12} = -10.0\%$ and $\Delta_{23} = +3.0\%$, consistent with the experimental values of $\Delta_{12} = -10.0 \pm 2.5\%$ and $\Delta_{23} = 0.0 \pm 2.5\%$ (Ref. 66), and theoretical results using the linearized augmented plane wave (FLAPW) method,⁶⁷ yielding $\Delta_{12} = -9.7\%$ and $\Delta_{23} = +3.6\%$.

Our calculated work functions for clean Cu(100) and Cu(110) surfaces are 4.39 and 4.18 eV, respectively, which are in reasonable agreement with the experimental values of 4.59 and 4.48 eV.⁶⁴ Earlier theoretical results include those of Skriver and Rosengaard⁷¹ who calculated values of 5.26 and 4.48 eV using linear muffin-tin orbitals and the local density approximation (LDA). Tao *et al.*⁶⁵ report a work function of 4.49 eV for Cu(100) using DFT-GGA in good agreement with our value of 4.39 eV. We note that the work functions of metal surfaces are usually underestimated by DFT-GGA calculations.⁶⁷

Our calculated surface energies for Cu(100) and Cu(110) are 0.64 and 0.97 eV per surface unit cell, respectively. These results correlate well with the FLAPW calculations of Da Silva *et al.*^{72,73} reporting surface energies of 0.60 eV for Cu(100) and 0.90 eV for Cu(110). The more approximate LDA muffin tin calculations of Skriver and Roosengard⁷¹ yield 0.85 and 1.33 eV, respectively.

B. Oxygen adsorption on Cu(100)

Cu sublattices and O binding sites. We examine oxygen adsorption on three types of Cu(100) surface structures (Fig. 1). The first structure is the simple, nonreconstructed Cu(100) surface shown in Fig. 1(a) which defines the (1×1) surface unit cell of this crystal face. On this surface there are three distinct high-symmetry adsorption sites: The *top* site (*T*) is located directly on top of a surface Cu atom, the *bridge* site (*B*) is a twofold coordinated site between two Cu atoms, and the *hollow* site (*H*) is coordinated by four Cu atoms. The second surface structure [Fig. 1(b)] is a missing-row reconstruction with a $(2\sqrt{2} \times \sqrt{2})R45^\circ$ unit cell,^{14,16,19,20,23} which features a chain of Cu atom vacancies in the $[011]$ direction. On this reconstruction the most favorable adsorption site is the *pseudohollow* site (pH), which is similar to the hollow site on the clean surface, but only threefold coordinated due to the missing row of Cu atoms. The third structure prototype is the distributed vacancy reconstruction (not shown in Fig. 1), which is closely related to the missing-row reconstruction, but is characterized by a nonordered, random distribution of Cu vacancies in the surface. The importance of the vacancy order/disorder transition was

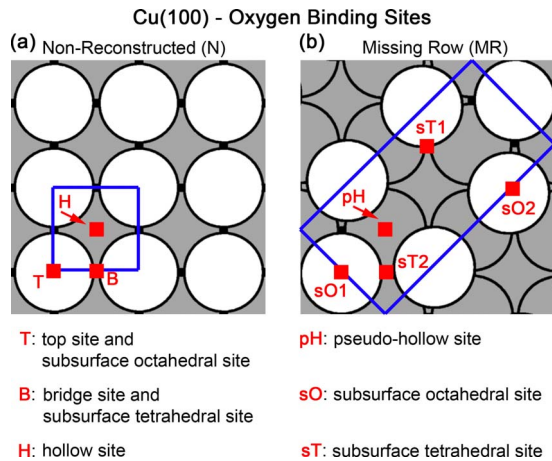


FIG. 1. (Color online) Oxygen binding sites on the Cu(100) surface showing in (a) the nonreconstructed (n) surface, and in (b) the missing-row (MR) reconstructed surface. Top-layer Cu atoms are white and second layer Cu atoms are gray. The in-plane position of surface and subsurface binding sites are indicated by red squares and labeled below the diagram.

highlighted by the work of Iddir *et al.*³³ and we will be using their $(2\sqrt{2} \times 2\sqrt{2})R45^\circ$ quasi-disordered model of this surface to study oxygen binding at the pseudohollow sites (pH). Additionally, for nonreconstructed and missing-row surfaces, we will be exploring subsurface binding sites which are indicated in Fig. 1. In the following discussion, we will use prefixes *N*-, *MR*-, and *DV*- with our unit cell notation to indicate nonreconstructed, missing row, and distributed vacancy reconstructions, respectively.

Oxygen on the nonreconstructed surface. We first consider the adsorption of oxygen on the three high-symmetry sites (top, bridge, and hollow) of the nonreconstructed surface (*N*) for a range of coverages. For each structure, we optimize the geometry and calculate the average oxygen binding energy, the work function change, and the surface dipole moment. The calculated binding energies are plotted in Fig. 2 and are listed for selected structures in Table I. For coverages of 0.5 ML and above, the binding energy decreases almost linearly with coverage indicating a gradual build-up of repulsive interactions between the adsorbed oxygen atoms.^{28,76} The highly coordinated hollow site (red data points) is energetically preferred at all coverages, and top site adsorption is always endothermic (i.e., $E_b^O < 0$). The bridge site is less stable than the hollow site by approximately 0.8 to 0.9 eV. For the energetically preferred hollow site, we have additionally investigated a lower coverage of 1/8 ML but find only a marginal change in the binding energy relative to the 1/4 ML result. This suggests that at these low coverages the interaction between oxygen adatoms is effectively screened.

Included in our nonreconstructed surfaces is a $c(4 \times 6)$ structure with a hollow-site oxygen coverage of 1/3 ML. This structure is inspired by earlier work,⁷⁷ which shows this structure to be thermodynamically stable on the Ag(100) surface. For the equivalent Cu(100) structure the stability is not as clear—as shown in Fig. 2, the average oxygen binding energy of the $c(4 \times 6)$ is very slightly smaller (i.e., less stable) than the linear combination of our $N-(2 \times 2)$ 1/4 and

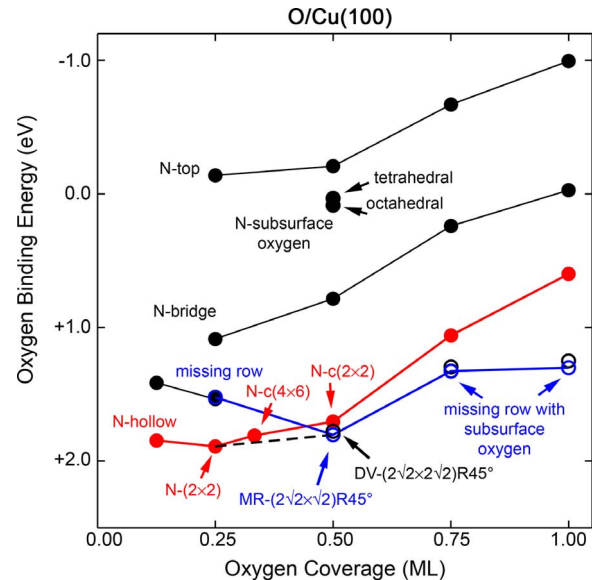


FIG. 2. (Color online) Calculated average binding energy per oxygen atom on Cu(100) in the on-surface and subsurface sites, for various coverages. The solid lines connecting the calculated binding energies are used to guide the eye. The dashed line indicates, as a guide to the eye, the convex hull connection between the 1/4 ML nonreconstructed surface and the 1/2 ML missing-row reconstruction.

$N-c(2 \times 2)$ 1/2 ML hollow-site structures. The average oxygen binding energies is 1.81 eV for the $c(4 \times 6)$, to be compared with 1.83 eV for the linear combination of $N-(2 \times 2)$ 1/4 and $N-c(2 \times 2)$ 1/2 ML. This is just within the error of our calculations due to slab thickness effects.

For a coverage of 1/2 ML we also consider subsurface binding of oxygen on the nonreconstructed surface. Two sites were tested: the tetrahedral subsurface site [see Fig. 1(a)], which is located directly under the surface bridge site, between the first and second atomic layers, and the octahedral site directly under the surface top site in the second layer. Our calculations show that oxygen atoms in these subsurface sites are much less stable than the on-surface hollow and bridge sites as shown in Fig. 2. Overall, our binding energy results are in qualitative and quantitative agreement with the previous GGA calculations of Kangas *et al.*²⁹

We note in passing that the binding of oxygen to Cu(100) is significantly stronger than to Ag(100). For 1/2 ML hollow-site adsorption on Ag(100), Cipriani *et al.*⁷⁴ and Gajdoš *et al.*⁷⁵ report GGA binding energies of 0.74 and 0.71 eV, respectively. This is less than half of the 1.71 eV binding energy that we find for Cu(100).

Oxygen on missing row and disordered vacancy reconstructions. Evidence from STM (Ref. 16) and diffraction¹⁷ experiments suggest the formation of a $(2\sqrt{2} \times \sqrt{2})R45^\circ$ reconstruction when the oxygen coverage reaches 1/2 ML. Shown in Fig. 3(b), this reconstruction is characterized by a missing row of copper atoms with 1/2 ML oxygen atoms adsorbed at the pseudohollow sites (pH) alongside the missing row. In order to evaluate the stability of these missing-row reconstructions, we consider a number of variants of the $(2\sqrt{2} \times \sqrt{2})R45^\circ$ structure. One variant reconstruction with a

TABLE I. Calculated structural parameters for different O coverage (from 1/8 to 1 ML) on Cu(100) in the hollow site. The values of oxygen adsorbed on the missing-row (MR) reconstructed surface for 1/4 and 1/2 ML are included for comparison. The binding energy, E_b^O , is calculated with respect to the isolated oxygen molecule. $d_{\text{Cu-O}}$ indicates the average bond length between oxygen and the nearest copper atom. d_{O1} is the minimum vertical height of O with respect to the surface Cu layer, Δ_{ij} ($i=1,3, j=2,4$) represents percent change relative to the bulk interlayer spacing, between the i th and j th atomic interlayer, where the center-of-mass of the layer is used. Also given are the workfunction change, $\Delta\Phi$, and the corresponding surface dipole moment, μ .

Structure	$N-(4\times 4)$ 1/8 ML	$N-(2\times 2)$ 1/4 ML	MR- $(4\sqrt{2}\times 2\sqrt{2})\text{R}45^\circ$ 1/4 ML	$N-(2\times 2)$ 1/2 ML	MR- $(2\sqrt{2}\times 2\sqrt{2})\text{R}45^\circ$ 1/2 ML	$N-(2\times 2)$ 3/4 ML	$N-(1\times 1)$ 1 ML
$d_{\text{Cu-O}}$ (Å)	2.01	2.01	1.86	1.96	1.86	1.95	1.89
d_{O1} (Å)	0.81	0.82	0.13	0.71	0.18	0.68	0.51
Δ_{12} (%)	+1.1	+0.6	+6.0	+5.0	+4.4	+14.3	+18.7
Δ_{23} (%)	+0.5	+0.4	+2.2	+1.1	+2.2	+6.0	-1.7
Δ_{34} (%)	+0.6	+0.6	+0.6	+0.6	+1.1	+0.6	+1.1
E_b^O (eV)	1.85	1.89	1.53	1.71	1.81	1.06	0.60
$\Delta\Phi$ (eV)	0.37	0.74	0.05	0.92	0.32	1.31	1.51
μ (Debye)	0.52	0.52	0.03	0.32	0.11	0.31	0.27

reduced oxygen coverage (1/4 ML) is created using a doubled unit cell, MR- $(4\sqrt{2}\times 2\sqrt{2})\text{R}45^\circ$, in which only half of the pseudohollow sites are occupied by oxygen. Missing-row structures with increased coverage (3/4 and 1 ML) are created in the $(2\sqrt{2}\times \sqrt{2})\text{R}45^\circ$ unit cell by placing additional oxygen atoms into subsurface tetrahedral or octahedral sites. The in-plane position of the subsurface sites are labeled as shown in Fig. 1(b) where sT1 and sT2 are tetrahedral sites, and sO1 and sO2 are octahedral sites. For 3/4 ML coverage, two reconstructions were considered: The tetrahedral reconstruction contains oxygen at the sT1 subsurface site, and the octahedral reconstruction has one oxygen at the sO1 site. We also construct tetrahedral and octahedral subsurface reconstructions for 1 ML coverage. The tetrahedral reconstruction has two oxygen atoms at two sT2 subsurface sites, the octahedral reconstruction has one oxygen atom each at sO1 and sO2 sites.

We now compare the energetics of the missing-row reconstructions to those of the nonreconstructed surface at the

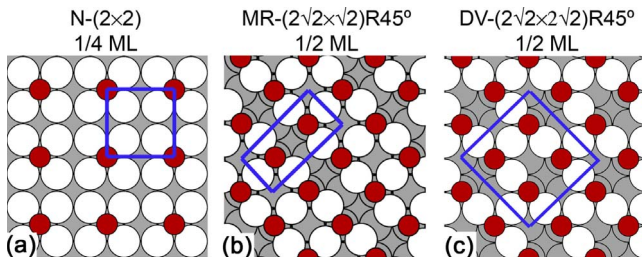


FIG. 3. (Color online) Top views of the favorable oxygen adsorption structures on Cu(100): (a) 1/4 ML oxygen coverage on a nonreconstructed surface with a (2×2) unit cell, (b) the missing row $(2\sqrt{2}\times \sqrt{2})\text{R}45^\circ$ reconstruction with 1/2 ML coverage, and (c) the “disordered vacancy” $(2\sqrt{2}\times 2\sqrt{2})\text{R}45^\circ$ structure that becomes stable at high temperature due to configurational entropy. Large white and gray spheres represent top layer Cu atoms and underlying substrate Cu atoms, respectively. Black (red) spheres represent O atoms. The rectangles (blue) indicate the supercells used in the calculations.

same coverage (see Fig. 2). For 1/4 ML coverage, the average oxygen binding energy of the missing-row $(4\sqrt{2}\times 2\sqrt{2})\text{R}45^\circ$ structure is 0.36 eV less stable, suggesting that a missing-row reconstruction is not preferred at this low coverage. However, this preference reverses when we consider higher coverages. At 1/2 ML, we find for the MR- $(2\sqrt{2}\times \sqrt{2})\text{R}45^\circ$ structure an oxygen binding energy that is 0.11 eV more favorable than that of the $N-c(2\times 2)$ structure. For 3/4 and 1 ML oxygen coverages, the missing-row reconstructions are also more stable than the nonreconstructed Cu(100) surface; however, the average oxygen binding energies are somewhat smaller relative to the 1/2 ML case, probably due to the less favorable subsurface oxygen binding sites involved. Overall, our results are consistent with the STM experiments of Fujita *et al.*²³ who report a $(2\sqrt{2}\times \sqrt{2})\text{R}45^\circ$ missing-row phase only for higher coverages.

Iddir *et al.*³³ recently made the convincing argument that the experimentally observed $(2\sqrt{2}\times \sqrt{2})\text{R}45^\circ$ to $c(2\times 2)$ transition at 475 K is due to an order-disorder phase transition involving the Cu vacancies that make up the missing row. They propose that above 475 K, the vacancies in the Cu sublattice become disordered, such that the apparent symmetry in the diffraction is determined by the 1/2 ML oxygen sublattice with a $c(2\times 2)$ unit cell.

In our calculation, we use the same 1/2 ML disordered vacancy (DV) structure [Fig. 3(c)] that Iddir *et al.*³³ employ to represent this surface (referred to as a “spaced vacancy structure” in Ref. 33). This structure has a $(2\sqrt{2}\times 2\sqrt{2})\text{R}45^\circ$ unit cell and arises by shifting every other Cu atom from a complete row into the missing row, thereby effectively creating a surface with two half-missing rows. The calculated average oxygen binding energy for this structure is 1.78 eV, which is 0.02 eV less than for the missing-row structure with ordered Cu vacancies. The energy difference per Cu vacancy is 0.058 eV, from which we can estimate, via the configurational entropy (see Ref. 33 for details), a transition temperature of 300 K between the ordered MR- $(2\sqrt{2}\times \sqrt{2})\text{R}45^\circ$ and the quasi-disordered $(2\sqrt{2}$

$\times 2\sqrt{2}R45^\circ$ [i.e., the observed $c(2\times 2)$ pattern]. Within the errors of our methodology, this compares reasonably well with the results of Iddir *et al.*³³ who report an experimental transition temperature of 475 K. Their DFT-GGA calculations give an energy difference of 0.13 eV (per Cu vacancy) and a transition temperature of 650 K. While the temperature variation is considerable due to the small energy differences involved, it is comforting to see that the experimental temperature lies in between the theoretical results of Iddir *et al.*³³ and the present work.

Surface Relaxations. We now consider the atomic structure of various surfaces which are listed in Table I. For the nonreconstructed (N) surface, we see that an increase in the oxygen coverage from 1/4 to 1 ML results in a decrease in the vertical position, d_{O1} , of oxygen above the surface plane from 0.81 to 0.51 Å. Similarly, the Cu–O bond length decreases from 2.01 to 1.89 Å. Our interlayer separations are in excellent agreement with the experimentally observed values which range from 0.4 to 0.8 Å depending on coverage.^{21,24} Below 1/4 ML coverage, we find no appreciable change in these properties. Overall, the coverage-dependent changes in the structural parameters match the trends seen in the binding energy. These trends are consistent with a reduction in the oxygen-oxygen repulsion with reduced coverage. The generally lower binding energies found for high coverages can thus be understood as due to the increased O–O repulsion. We believe the hollow site preference arises, because O–O repulsion is partly screened by the short Cu–O bond lengths. At low coverage, the electrostatic interaction between O adatoms is less effective, so that the distance between the adatoms and the metal surface becomes larger.

Oxygen adsorption results in significant relaxations in the first and second atomic layers with a concomitant change in the calculated interlayer spacing. For the clean surface, Δ_{12} is negative (−2.3%) corresponding to a small contraction between the first and second layers relative to the bulk value. With 1 ML of oxygen at the hollow site, Δ_{12} becomes strongly positive (+18.7%) corresponding to a significant expansion. With decreasing oxygen coverage, the interlayer spacing gradually decreases toward the clean surface value. The oxygen-induced expansion can be understood as a charge transfer from copper to oxygen atoms resulting a depletion of the electron density between the first and second Cu layer and a weakening of the bonding. This is broadly analogous to what has been reported for oxygen on palladium and other metallic surfaces.^{74,78}

The obtained structural parameters for the 1/4 and 1/2 ML missing-row reconstructions are listed in Table I. At 1/2 ML coverage, the oxygen atoms are located at a height of 0.18 Å above the outmost Cu layer, which is comparable to the value of 0.28 Å from other DFT-GGA calculations using the pseudopotential method and a plane wave basis.³¹ The experimental value is 0.17 ± 0.1 Å from a photoelectron diffraction study,²⁴ and 0.1 Å (Ref. 22) by LEED. The calculated bond lengths to the four coordinating Cu atoms are 1.88, 1.86, 1.86 and 2.24 Å, close to the experimental values 1.80, 1.83, 1.83, and 2.12 Å, respectively.²²

Electronic structure. We now turn to the electronic properties of the O/Cu(100) system. Figure 4 shows the changes

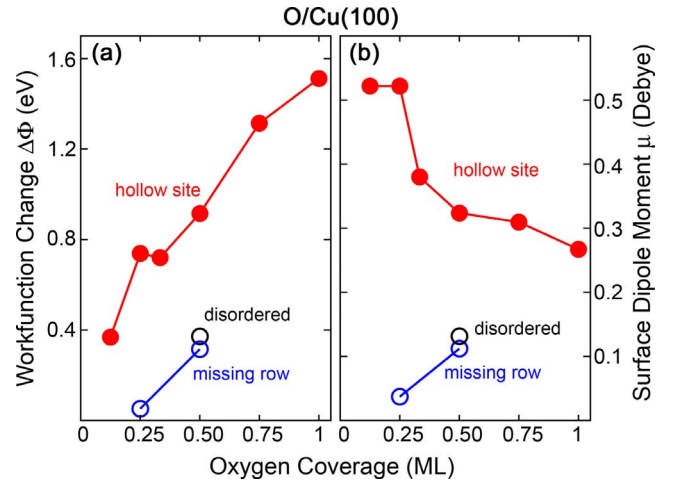


FIG. 4. (Color online) Calculated work function change, $\Delta\Phi$, and surface dipole moment, μ , as a function of coverage for O on Cu(100). The solid lines connecting the calculated values are to guide the eye.

in the work function and surface dipole moment as a function of the oxygen coverage. For hollow-site adsorption and the missing-row reconstructions we can see that the work function change $\Delta\Phi$ increases monotonically with coverage. This can be understood in terms of the large surface dipole moment arising due to partial electron transfer from the substrate to the adsorbate; the difference between the electronegativity of oxygen (3.44) and copper (1.90) is quite large (1.54). With increasing coverage, a repulsion builds up among the partially negatively charged O atoms. To reduce this repulsion, there will be partial electron transfer back to the substrate, giving rise to a decrease in the surface dipole moment, resulting in a depolarization. The missing-row reconstructed surfaces exhibits similar trend with coverage. We note at this point that the work function change for O/Cu(100) behaves differently to what has been reported for the O/Ag(100) system.⁷⁵ For Ag(100), the work function increases up to 1/2 ML and then decreases due to negative adsorption heights at high coverage. Negative adsorption heights do not occur in our Cu(100) structures. This may be due to the 12% smaller lattice constant of Cu compared to Ag.

Further insights into the electronic structure are gained from the electron density difference distributions and projected density of states (PDOS). We show in Fig. 5 the electron density difference (relative to the clean surface) for a plane perpendicular to the surface for the N - $p(2\times 2)$ 1/4 ML and the MR- $(2\sqrt{2}\times\sqrt{2})R45^\circ$ structures. We see that the perturbation caused by O adsorption is mostly localized at the oxygen atom and the topmost layer of Cu atoms. The electron density around the oxygen adatom is enhanced and is depleted around the Cu atoms. The electron transfer from Cu to the O adatom is reflective of the relative electronegativities of the two elements.

The projected densities of states presented in Fig. 6 for the N - $c(2\times 2)$ 1/2 ML and the MR- $(2\sqrt{2}\times\sqrt{2})R45^\circ$ 1/2 ML structures, where the O-2*p* and Cu-3*d* orbitals are shown. It can be seen that there is a hybridization between the O-2*p*

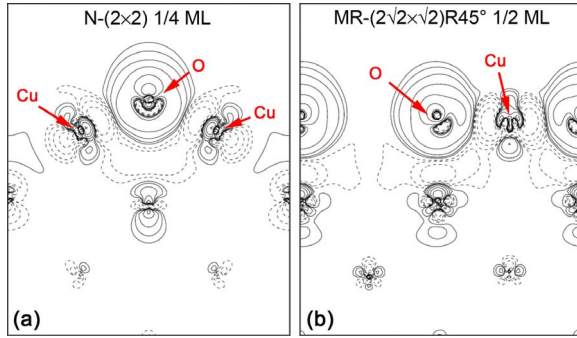


FIG. 5. (Color online) Difference electron density distribution of O/Cu(100) structures: (a) The nonreconstructed (2×2) structure with a $1/4$ ML coverage of oxygen at the hollow site. (b) The missing row $(2\sqrt{2} \times \sqrt{2})R45^\circ$ reconstruction with a coverage of $1/2$ ML. Solid and dashed isolines indicate lines of constant charge accumulation and depletion, respectively. The lowest positive contour line is at 0.001 electron Bohr $^{-3}$, while the highest negative contour line corresponds to a value of -0.001 electron Bohr $^{-3}$. Successive isolines differ by a factor of $10^{1/3}$.

and Cu-3d in the energy range -7 to -5 eV. The greater occupation of hybridized O-2p and Cu-3d bonding states compared to antibonding states, reflects the relatively strong Cu-O bond. The nature of the states in the PDOS is confirmed (not shown) by the single particle wave function at the chosen eigenstates at the Γ point. The eigenvalues corresponding to low energies are due to bonding states, while those close to the Fermi level are due to antibonding states. Furthermore, surface Cu-3d states are narrowed compared to subsurface Cu-3d states due to reduced coordination at the surface. For the MR- $(2\sqrt{2} \times \sqrt{2})R45^\circ$ $1/2$ ML structure, the bonding states of O-2p extend to 8 eV below the Fermi level, and the occupancy of the antibonding states is lower than that of the N- $c(2 \times 2)$ $1/2$ ML system, which indicates the stronger interaction between O and surface Cu atoms in the reconstructed system.

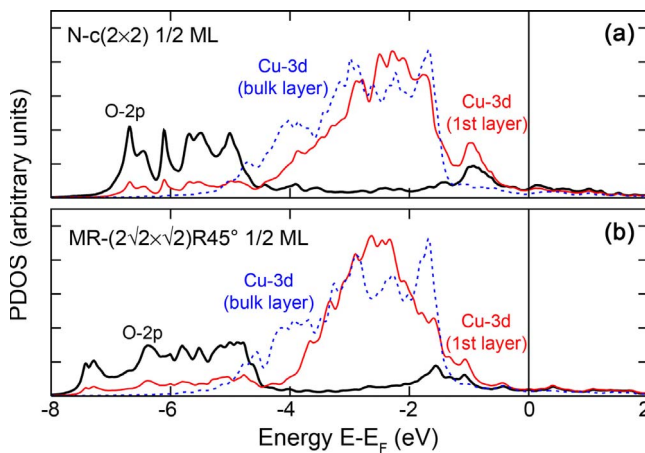


FIG. 6. (Color online) Projected density of states (PDOS) for the selected O/Cu(100) structures with $1/2$ ML oxygen coverage: (a) The nonreconstructed $c(2 \times 2)$ and (b) the missing row $(2\sqrt{2} \times \sqrt{2})R45^\circ$ structure. Energies are given relative to the Fermi level E_F . The bulklike Cu-3d PDOS of atoms in the center of the slab is indicated using a dotted line.

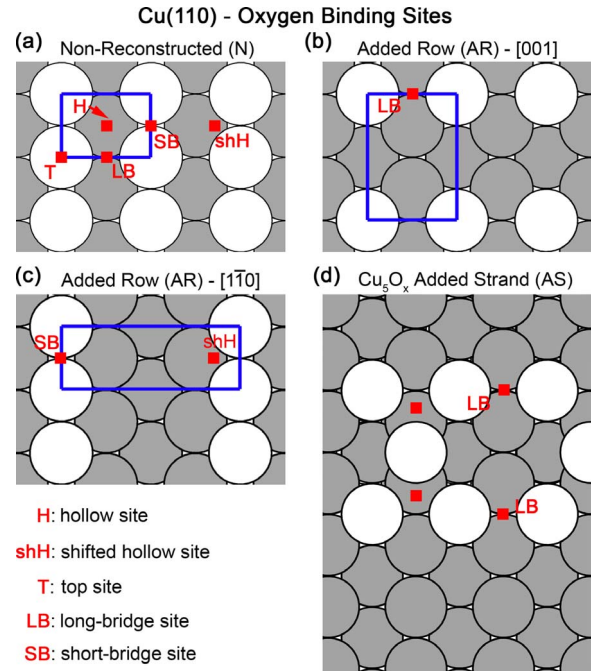


FIG. 7. (Color online) Oxygen binding sites on the Cu(110) surface showing (a) the nonreconstructed (n) surface, (b) the $[001]$ added row (AR) reconstructed surface with a (2×1) unit cell, (c) the $[1\bar{1}0]$ added row (AR) surface with a (1×2) unit cell, and (d) a Cu_5O_x added strand (AS) on the nonreconstructed surface. A close packing of Cu_5O_4 added strands gives rise to the $2/3$ ML $c(6 \times 2)$ reconstruction at high oxygen exposures. Top-layer Cu atoms are colored white and second layer Cu atoms are colored gray. The in-plane position of surface and subsurface binding sites are indicated by red squares and labeled below the diagram.

C. Oxygen adsorption on Cu(110)

Cu sublattices and O binding sites. Being characterized by a rectangular surface unit cell, the Cu(110) surface offers, relative to the square unit cell Cu(100), a larger number of possibilities for oxygen adsorption. On the nonreconstructed surface [Fig. 7(a)], we have five distinct sites. The *hollow site* (H) is located above the center of four surface Cu atoms. The *long-bridge* (LB) and the *short-bridge* (SB) sites are located between pairs of surface Cu atoms along the $[001]$ and $[1\bar{1}0]$ directions, respectively. The *shifted-hollow* (shH) site is pseudo threefold coordinated and located roughly halfway between hollow and short-bridge sites. Oxygen adsorption at the *top site* (T) directly above a surface Cu atom has previously been shown to be unstable⁴⁷ and is not further explored here. We also consider two types of *added row* (AR) reconstructions [Figs. 7(b) and 7(c)] in which rows of Cu atoms are added along the $[001]$ and the $[1\bar{1}0]$ directions. We consider these rows at different separations using (2×1) , (4×1) , and (8×1) unit cells for rows in the $[001]$ direction, and a (1×2) unit cell for the $[1\bar{1}0]$ direction. Added row structures with a (1×1) periodicity are equivalent to a nonreconstructed surface. For the $[001]$ added row structures, we consider oxygen binding at the long-bridge site of the added row as illustrated in Fig. 7(b). For the $[1\bar{1}0]$ added row, we investigate oxygen binding at short bridge and

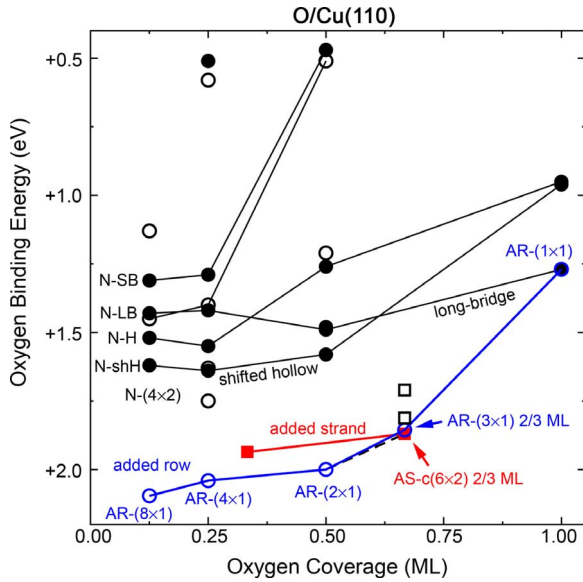


FIG. 8. (Color online) Calculated average binding energy of oxygen on Cu(110) for various coverages and configurations. The dashed line connects the binding energies of the most stable structures and serves to guide the eye.

shifted hollow sites [see Fig. 7(c)]. Finally, we consider reconstructions that we describe as *added strand* structures (AS) in which Cu adatoms are arranged into strands as illustrated in Fig. 7(d). On this surface oxygen binds to the two long-bridge sites and also to two threefold sites, forming a Cu_5O_4 -stoichiometric added strand that is the basic building block of an experimentally observed $c(6 \times 2)$ reconstruction. We will examine several variations in this pattern that differ in the relative alignment of nearby strands or the number of Cu atoms within the strand. In our structure notation, we use prefixes *N*-, *AR*-, *AS*- to indicate the Cu-sublattice as nonreconstructed, added row, or added strand, respectively. An overview of our calculated average oxygen binding energies for these sublattices and a range of oxygen coverages between 1/8 and 1 ML is given in Fig. 8.

Oxygen on the nonreconstructed surface. For low coverage (1/8 ML) on the nonreconstructed surface oxygen is preferentially bonded to the shifted-hollow site (labeled N-shH in Fig. 8), followed in order of decreasing stability by the hollow, the long-bridge, and the short-bridge sites. At 1/8 ML, our calculated binding energy of the shifted hollow site is 1.62 eV, which is in good agreement with the earlier result of 1.59 eV reported by Liem *et al.*⁴⁷ At a coverage of 1/2 ML, the shifted-hollow site is still the preferred structure, however the long-bridge site is now the second most stable structure. This order is reversed above ≈ 0.6 ML coverage, and the long-bridge site becomes the preferred binding site. The general trend on the nonreconstructed surface is that at a coverage of 1/4 ML and above, the binding energies begin to rapidly decrease, which again reflects the increased repulsion between an increasing number of oxygen atoms on the surface.^{28,76} The long-bridge site is an exception to this trend, showing the least variation in the binding energy with oxygen coverage.

Added row reconstructions. The average binding energies

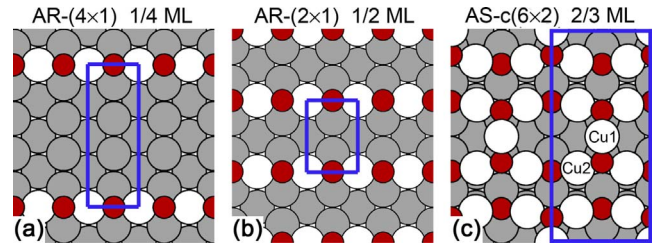


FIG. 9. (Color online) Top views of the favorable oxygen adsorption structures on Cu(110). Shown are (a) the 1/4 ML oxygen coverage added row (4×1) structure characterized by Cu-O-Cu-O-Cu chains in the $[100]$ direction, (b) the added row (2×1) structure with 1/2 ML coverage with a closer spacing of the CuO chains, and (c) the $c(6 \times 2)$ structure with 2/3 ML oxygen coverage composed of Cu_5O_4 added strands in the $[100]$ direction. Large white and gray circles represent top and second layer Cu atoms, respectively. Small dark (red) circles represent O atoms. The rectangles indicate the surface unit cells used in the calculations. In the $c(6 \times 2)$ structure, the nonequivalent Cu atom sites Cu1 and Cu2 are indicated (see Table III).

(Fig. 8) show that added row reconstructions are preferred over most of the oxygen coverage range. The most stable reconstructions are characterized by $[001]$ added rows (blue data points in Fig. 8) in which oxygen atoms occupy all of the long-bridge sites. This creates continuous Cu-O-Cu-O-Cu adatom chains that appear to be particularly stable which is evident by the fact that a reduced oxygen coverage does not disrupt these chains. Instead the reduced availability of oxygen atoms is accommodated by an increased average separation between the Cu-O rows, as illustrated in Figs. 9(a) and 9(b) for the 1/4 and 1/2 ML structures, respectively.

For the 1/2 ML $[001]$ added row structure, our calculated oxygen binding energy is 2.00 eV, which is in good agreement with the previously reported values of 2.11 and 2.03 eV by Liem *et al.*⁴⁷ and Frechard *et al.*,⁴⁶ respectively. Oxygen adsorption at the short-bridge site of a $[1\bar{1}0]$ added row structure [Fig. 7(c)] is considerably less stable, with a calculated binding energy of only 1.29 eV. The shorter bridge causes the oxygen adatoms to be displaced higher above the adatom row, which presumably results in less effective screening and increased repulsion between oxygen atoms.

For the stable $[001]$ AR structures, the average oxygen binding energies do not change much when the coverage decreases below 1/2 ML; for example, 1/4 ML and 1/8 ML coverages have binding energies of 2.04 and 2.07 eV, to be compared with 2.00 eV for 1/2 ML. This indicates that the Cu-O rows are only very weakly repulsive when separated by more than one lattice unit; however, above 1/2 ML the binding energies decrease rapidly to 1.71 eV for 2/3 ML and 1.27 eV for 1 ML. In this coverage regime, the Cu-O adatom rows are separated by less than two lattice units on average, meaning that a larger number of rows are brought into single lattice unit separation; the energetics suggests that this an unfavorable arrangement. For a full 1 ML coverage, the surface is so densely packed with Cu-O adatom rows that the Cu-sublattice is in fact identical to the nonreconstructed surface [Fig. 7(a)] in which oxygen atoms occupy all of the long bridge sites.

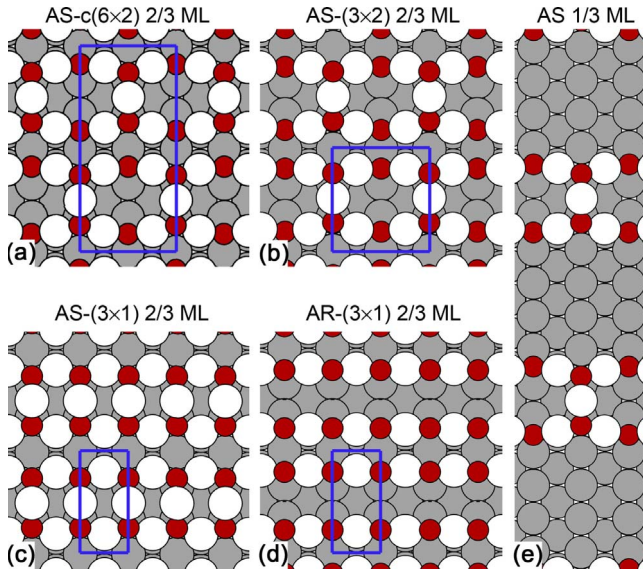


FIG. 10. (Color online) Variations in added strand reconstructions on Cu(110). (a) The experimental $c(6 \times 2)$ reconstruction which is composed of Cu_5O_4 added strands, (b) a (3×2) variant in which the bridging Cu atoms are not shifted between adjacent strands, (c) a (3×1) variant of Cu_3O_2 stoichiometry, containing a full row of bridging Cu atoms, and (d), for comparison, a $2/3$ ML CuO added row structure. Panel (e) shows a $1/3$ ML added strand structure formed by removing every other strand from the $c(6 \times 2)$ structure. Large white and gray circles represent top and second layer Cu atoms, respectively. Small dark (red) circles represent O atoms. The rectangles indicate the surface unit cells used. Note that the unit cell for the $c(6 \times 2)$ structure is shifted away from centered to facilitate comparison with the other unit cells.

The added strand reconstructions. Experimental evidence⁵² points to the existence of a $c(6 \times 2)$ reconstruction at oxygen coverages above $2/3$ ML. This reconstruction was attributed by Feidenhans'1 *et al.*⁵⁰ to the $2/3$ ML oxygenated added strand structure shown in Fig. 10(a). In our calculations, we find that this reconstruction has a binding energy of 1.87 eV, which is marginally more stable than the $2/3$ ML added row structure [Fig. 10(d), $E_b^O = 1.86$ eV]. The $c(6 \times 2)$ reconstruction is a Cu_5O_4 added strand structure that differs from the $[001]$ added row structures by having additional Cu atoms placed between pairs of Cu-O added rows. These Cu atoms cross link between every other pair of oxygen atoms within the two rows, thereby creating a strand structure that is oriented along the $[001]$ direction and has a width of three lattice units in the $[1\bar{1}0]$ direction. In the $c(6 \times 2)$ reconstruction, these strands are closely packed, and the linking Cu atoms are shifted by one $[001]$ lattice unit from one strand to the next. An alternative (3×2) added strand structure [Fig. 10(b)] is slightly less stable with an average oxygen binding energy of 1.82 eV. This structure is similar to the $c(6 \times 2)$ reconstruction but the linking Cu atoms are not shifted from one strand to the next. In a second variant, shown in Fig. 10(c), we tested the stability of a (3×1) added strand reconstruction in which all oxygen atom pairs are cross-linked by Cu atoms. With an average oxygen binding energy of 1.71 eV, this structure is also less stable than the $c(6 \times 2)$.

It is worthwhile to briefly reflect on the energetic proximity of the four $2/3$ ML structures [Figs. 10(a)–10(d)] considered here and the significance of these results in relation to experiment. Within the computational errors of our procedure (≈ 0.01 eV in binding energies), the AS- $c(6 \times 2)$ and the AR- (3×1) are very nearly of the same energy. This is to say that the presence or absence of the $1/6$ ML bridging Cu atoms has only a very subtle effect on the stability of the surface. A further increase in the density of bridging Cu atoms to $1/3$ ML, which leads to the AR- (3×1) structure, produces a significant destabilization of 0.15 eV in the average oxygen binding energy. Also significant within the margins of error is the 0.05 eV difference in the oxygen binding energy between the two added-strand structures $c(6 \times 2)$ and (3×2) . These last two findings, suggest that the positioning of bridging Cu atoms is correlated both within and between adjacent strands. This in turn will prompt any bridging Cu atoms present to arrange into some local order. While the amount of bridging Cu atoms between 0 and $1/6$ ML is not significantly explained by our energetics, we may speculate that configurational entropy would favor structures that contain bridging Cu atoms over those that do not. This would not be dissimilar to the mechanism that stabilizes the $1/2$ ML disordered vacancy structure on the (100) surface.³³

Lastly, we also tested the stability of an isolated added strand as shown in Fig. 10(e) with an oxygen coverage $1/3$ ML. The calculated average oxygen binding energy is 1.94 eV. This is less stable than what we expect (by linear interpolation) for a $1/3$ ML added-row structure ($E_b^O = 2.03$ eV). Thus, it appears that the close proximity of (and repulsion between) the Cu-O adatom rows is an important ingredient in making the added strand structures competitive with the added row structures.

Structural Relaxations. Calculated interplanar separations for several relevant surface structures are listed in Table II. The internal coordinates of the two oxygen and two surface Cu atoms as indicated in Fig. 9(c) are listed in Table III. Our calculated results are in good agreement with the experimental values from low energy ion scattering (LEIS) measurements,⁵² improving over earlier effective-medium theory (EMT) calculations.³⁸

Figure 9(b) depicts the AR- (2×1) structure in which the O atoms occupy the long-bridge sites of every other $[001]$ copper row, while the other rows are missing. In this structure, the O atoms are bonded to two surface Cu atoms and two subsurface Cu atoms, where the Cu–O bond lengths are 1.83 and 2.05 Å, respectively. These values are in good agreement with the various experimental results which are in the range of 1.81–1.84 and 2.00–2.05 Å (Refs. 22, 43, 50, and 52) and with the findings of the first-principles calculations of Liem *et al.*⁴⁷ (1.83 and 2.08 Å) and of Frechard *et al.*⁴⁶ (1.83 and 2.05 Å). The vertical height of O, d_{O1} , is calculated to be 0.13 Å, which is larger than the LEED values ~ 0.03 Å^{22,43} but comparable to the value of 0.10 Å obtained by Frechard *et al.*⁴⁶ where only O atoms and the first Cu layer were optimized.

Electronic Structure. To elucidate the binding properties of oxygen on the Cu(110) surface we list the change in the work function and surface dipole moment for the most favorable oxygen structures in Table II. These values are also

TABLE II. Calculated structural and electronic parameters for different O coverages (from 0.125 to 0.5 ML) for the missing-row reconstructed Cu(110) surfaces. The binding energy, E_b^O is calculated with respect to the isolated oxygen molecule. $d_{\text{Cu-O}}$ indicates the average bond length between oxygen and the nearest copper atom. d_{O1} is defined to be the minimum vertical height of O with respect to the surface Cu layer, Δ_{ij} ($i=1,3$, $j=2,4$) represents the percent change in the i th and j th metal interlayer distances, where the center-of-mass of the layer is used, relative to the bulk interlayer spacing. $\Delta\Phi$ and μ represent the work function change and surface dipole moment, respectively.

Structure	AR-(8×1) 1/8 ML	AR-(4×1) 1/4 ML	AR-(2×1) 1/2 ML	AS-c(6×2) 2/3 ML
$d_{\text{Cu-O}}$ (Å)	1.98	1.97	1.97	2.09
d_{O1} (Å)	0.13	0.13	0.13	0.05
Δ_{12} (%)	+14.5	+12.5	+10.8	+23.1
Δ_{23} (%)	-10.0	-6.4	-1.5	-3.9
Δ_{34} (%)	+2.7	+0.5	-3.1	-1.5
E_b^O (eV)	2.07	2.04	2.00	1.87
$\Delta\Phi$ (eV)	0.20	0.33	0.56	0.54
μ (Debye)	0.40	0.33	0.27	0.20

plotted in Fig. 11. It can be seen that as more effective charges (i.e., oxygen atoms) are added to the surface, $\Delta\Phi$ increases with coverage from 1/8 to 1/2 ML, while the surface dipole moment decreases with coverage.

We plot the difference electron density for the two stable structures, AR-(2×1) and AS-c(6×2), in Fig. 12. It can be seen that the oxygen atoms appear to be almost coplanar with adjacent Cu atoms. Due to the large electronegativity of oxygen, the electron density of the oxygen atoms is enhanced, while the electron density of the nearest-neighbor Cu atoms is depleted. The slight accumulation of electron density toward the vacuum side of the surface results in an inward pointing surface dipole moment and a positive $\Delta\Phi$.

TABLE III. Atomic positions in Å of nonequivalent atoms of the added-strand c(6×2) 2/3 ML reconstruction. The results of this work are compared to the positions obtained by low-energy ion-scattering (LEIS) (Ref. 52) and effective-medium theory (EMT) (Ref. 32). In-plane coordinates are given relative to the Cu1 site [see Fig. 9(c)]. Coordinates not listed in the table are zero due to symmetry. The results of the present work use a rectangular unit cell of $a=7.2856$ Å and $c=15.455$ Å.

Atom		This work	EMT ^a	LEIS ^b
Cu1	z	0.55	1.2	$0.45 \pm .1$
Cu2	x	2.29	2.38	2.28
	y	1.78	1.805	1.78 ± 0.07
O1	x	1.85	1.36	1.78
	z	0.50	0.4	0.4 ± 0.1
O2	x	5.21	5.094	5.2 ± 0.1
	z	-0.06	-0.2	-0.12 ± 0.1

^aReference 70.

^bReference 57.

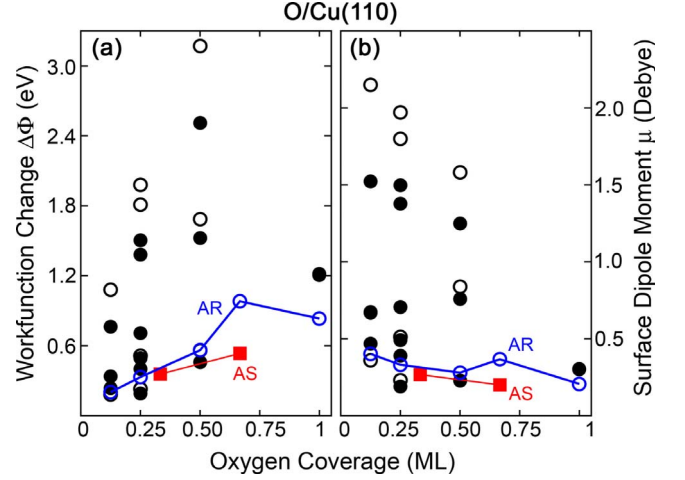


FIG. 11. (Color online) Calculated work function change, $\Delta\Phi$, and surface dipole moment, μ , as a function of coverage for O on the Cu(110) surface for the various structures considered. Solid lines connect the low-energy added row (AR) and added strand (AS) structures. Filled and open circles indicate the work functions of other nonreconstructed and reconstructed phases, respectively.

Figure 13 shows the PDOS of the O-2*p*, Cu-3*d* orbitals for the 1/2 ML oxygenated AR-(2×1) and the 2/3 ML AS-c(6×2) phases. In both cases, a renormalization of the O-2*p* states to lower energies is found. The hybridization of bonding states between the O-2*p* and Cu-3*d* orbitals is located mainly in the energy window from -4 to -8 eV. The corresponding antibonding states are located at -2 to 2 eV. Furthermore, the surface Cu-3*d* states in Figs. 13 are narrower than those of the bulk Cu-3*d* states, and this is again due to reduced coordination of surface Cu atoms.

IV. DISCUSSION

Having surveyed oxygen binding at varying coverages on Cu(100) and Cu(110), we are now in a position to assess the

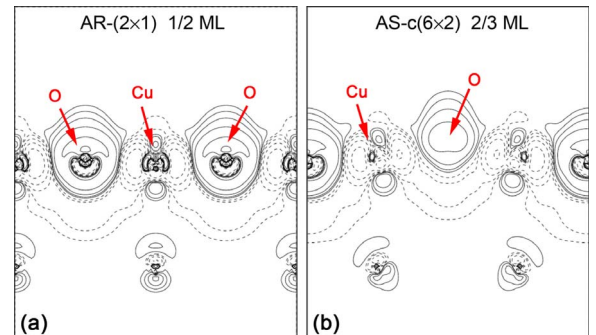


FIG. 12. (Color online) Difference electron density distribution of O/Cu(110) structures: Shown are (a) the added row (2×1) structure with a 1/2 ML oxygen coverage and (b) the added strand reconstructed c(6×2) structure with a 2/3 ML coverage. Dashed isodensity lines represent charge depletion relative to the clean surface and the solid isodensity lines depict charge accumulation. The lowest positive contour line is at 0.001 electron Bohr⁻³, while the highest negative contour line corresponds to a value of -0.001 electron Bohr⁻³. Successive isolines differ by a factor of 10^{1/3}.

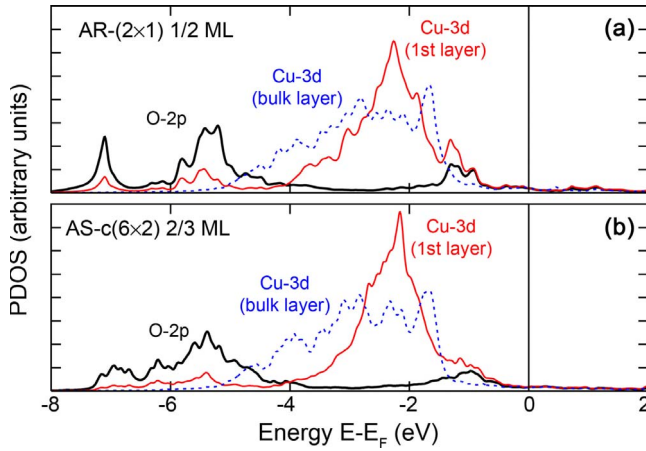


FIG. 13. (Color online) Projected density of states (PDOS) for selected O/Cu(110) structures showing (a) the added row (2×1) structure with 1/2 ML oxygen coverage and (b) the added strand $c(6 \times 2)$ structure with 2/3 ML coverage. Energies are given relative to the Fermi level E_F . The bulklike Cu-3d PDOS of atoms in the center of the slab is indicated using a dotted line.

relative stability of these structures when they are in thermodynamic contact with a real gas phase environment. Within the framework of *ab initio* atomistic thermodynamics a surface is assumed in thermodynamic equilibrium with both the gas phase above the surface and the bulk elemental solid (Cu) below. The gas phase is represented by the oxygen chemical potential $\Delta\mu_O(p, T)$ [given here relative to molecular O_2 as per Eq. (4)], which in turn is given by the gas phase oxygen partial pressure p and the temperature T . Under these conditions, the preferred surface for a given p and T is the one of lowest surface free energy γ and it is this surface that we should expect to observe experimentally at these conditions.

This type of analysis leads to the phase stability diagrams shown in Fig. 14 in which the free energies of the considered surface structures are plotted against the oxygen chemical potential $\Delta\mu_O$. In these diagrams, free energies are reported as differences $\Delta\gamma$ relative to the clean surface as defined in Eq. (3). Plotted in this way, individual surface structures appear as straight lines with a negative slope ($-N_O/2A$) that is proportional to the oxygen coverage. Critical for this discussion are the curves of minimum free energy (colored red in the online version) that form when the free energy lines of the most stable surfaces intersect one another. These points of intersection on the $\Delta\mu_O$ axis define the conditions of a phase transition from one minimum free energy surface to another. In this way, the $\Delta\mu_O$ scales for Cu(100) and Cu(110) are divided into several distinct segments in which different clean and oxygenated surface structures are preferred. These segments are indicated in Fig. 14 and are labeled by the type of the surface and the oxygen coverage in ML. An upper limit for $\Delta\mu_O$ exists at -1.24 eV. This corresponds to the calculated heat of formation of bulk Cu_2O which defines the point at which a bulk phase transition from Cu to Cu_2O will occur. In the limit of low oxygen exposure (i.e., large negative $\Delta\mu_O$), the clean Cu surface is preferred for both (100) and (110) crystal faces. In between these two limits, several

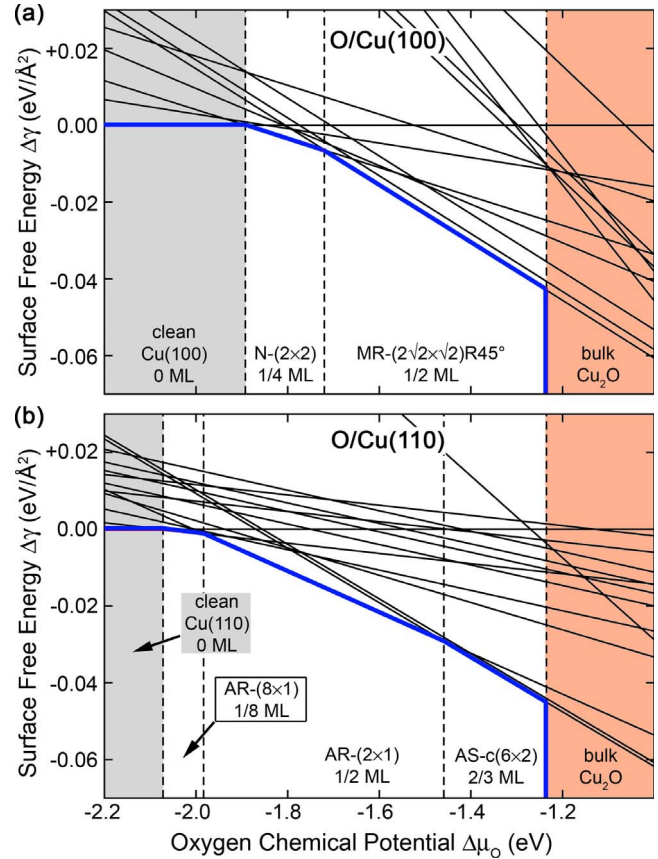


FIG. 14. (Color online) Calculated surface phase stability diagram for (a) the O/Cu(100) system and (b) the O/Cu(110) system as a function of the oxygen chemical potential. A thick (blue) line highlights the minimum free energy curve for each surface. Vertical dashed lines indicate the phase transition points on the $\Delta\mu_O$ axis. A shaded background on the left and right hand side denotes the regions of stability of the clean surface and the bulk oxide (Cu_2O), respectively. In between (without shading) are the surface oxide phases. Note that the free surface energy is reported as $\Delta\gamma$ relative to the respective clean (oxygen-free) surface.

oxygenated surface structures are found to be thermodynamically stable. We note in passing that at some oxygen potential above -1.24 eV a phase transition between bulk Cu_2O and bulk CuO is expected to occur. This transition was not further explored in this work as it occurs outside the $\Delta\mu_O$ limits relevant to surface oxide formation.

Starting with the clean Cu(100) surface [see Fig. 14(a)], an increase in $\Delta\mu_O$ leads at -1.89 eV to a phase transition to a $N-(2 \times 2)$ structure with an oxygen coverage of 1/4 ML. This oxygenated surface corresponds to the nonreconstructed, hollow-site adsorption structure that we found in Fig. 2 to be preferred for a 1/4 ML coverage. A further increase in the oxygen exposure results at $\Delta\mu_O = -1.72$ eV in another phase transition from the $N-(2 \times 2)$ 1/4 ML structure to the missing row ($2\sqrt{2} \times \sqrt{2}$) $R45^\circ$ reconstruction with a 1/2 ML coverage. This surface phase remains the preferred reconstruction until the bulk-oxide limit at $\Delta\mu_O = -1.24$ eV is reached. None of the higher coverage structures considered by us are thermodynamically stable anywhere on the $\Delta\mu_O$ scale.

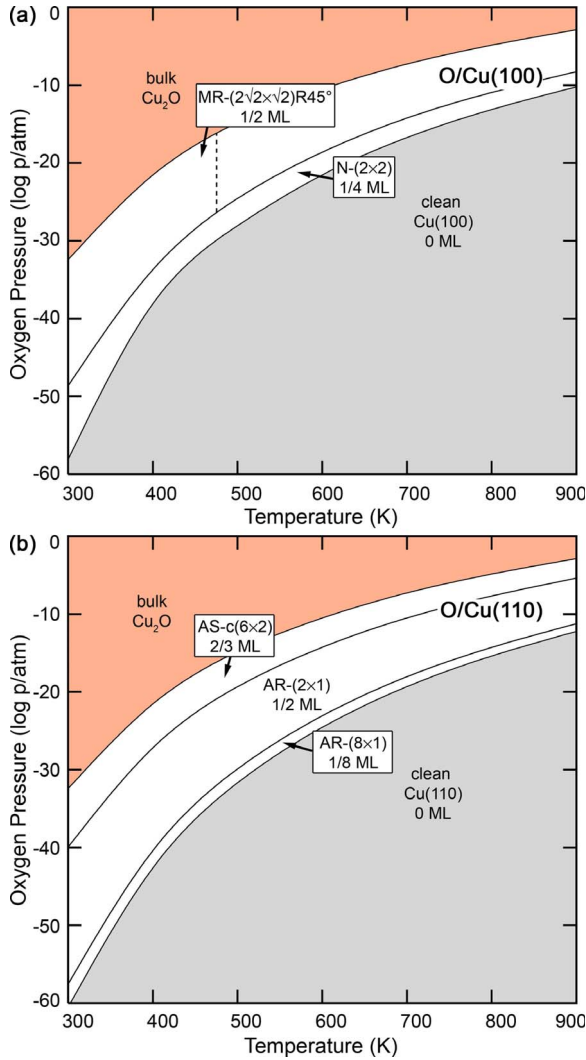


FIG. 15. (Color online) Stability of oxygen-free, surface-oxide, and bulk-oxide phases in a (p, T) phase diagram for (a) the O/Cu(100) and (b) the O/Cu(110) system, based on the $\Delta\mu_{\text{O}}$ phase boundaries determined in Fig. 14. The vertical dotted line in panel (a) indicates the experimental (Ref. 33) phase boundary at 475 K above which the Cu vacancies of the MR- $(2\sqrt{2} \times \sqrt{2})\text{R}45^\circ$ structure become disordered, giving rise to a disordered vacancy structure that appears as a $c(2 \times 2)$ reconstruction.

In the (p, T) phase diagram [Fig. 15(a)] the two $\Delta\mu_{\text{O}}$ segments corresponding to the stable surface oxides (white background) form a band of roughly 10 to 20 orders of magnitude width on the pressure scale and are bounded on the high and low pressure side by bulk Cu_2O and the oxygen-free surface, respectively. In the region corresponding to the MR- $(2\sqrt{2} \times \sqrt{2})\text{R}45^\circ$ 1/2 ML, we have additionally indicated the 473 K phase boundary³³ to the 1/2 ML disordered vacancy structure that is experimentally observed as a $c(2 \times 2)$ pattern. This results in a diagram with a total of four distinct surface phases: the clean Cu(100) surface at low oxygen pressure, a nonreconstructed (2×2) structure with 1/4 ML oxygen atoms at the hollow site at increased pressures, and then either the ordered missing row (for $T < 473$ K) or the disordered vacancy $c(2 \times 2)$ structure (for $T > 473$ K). While the MR- $(2\sqrt{2} \times \sqrt{2})\text{R}45^\circ$ to $c(2 \times 2)$ tran-

sition is well documented experimentally, there does not appear to be any evidence for a 1/4 ML structure with (2×2) symmetry (see e.g., the phase diagram Fig. 1 in Ref. 33). This is not necessarily a conflict. At coverages of around 1/4 ML (and below) our calculated oxygen binding energies on the nonreconstructed Cu(100) surface are very nearly constant with respect to changes in coverage (see Fig. 2). This implies that the oxygen adatoms in the $N-(2 \times 2)$ phase are weakly interacting, and plausibly, disordered distribution on the surface. Thus, the $N-(2 \times 2)$ 1/4 ML structure in our phase diagram acts as a “placeholder” for the low-coverage disordered arrangement of oxygen atoms on the nonreconstructed surface, which will appear as a (1×1) structure in experiment. Only when the oxygen exposure increases, and the surface progresses toward a 1/2 ML coverage, do the oxygen binding energies increase. This causes oxygen atoms to lock into an ordered $c(2 \times 2)$ 1/2 ML pattern. Thermodynamically, this structure supports the formation of Cu vacancies, which in turn may order into the MR- $(2\sqrt{2} \times \sqrt{2})\text{R}45^\circ$ 1/2 ML phase, or remain disordered in the DV- $c(2 \times 2)$ 1/2 ML phase.

Looking now at the Cu(110) surface, the phase stability diagram in Fig. 14(b) shows at $\Delta\mu_{\text{O}} = -2.07$ eV a transition of the oxygen-free surface into the added row (8×1) structure with a 1/8 ML oxygen coverage. At -1.98 eV, the added row (2×1) structure with 1/2 ML oxygen becomes favorable. This structure corresponds to a denser packing of the oxygenated added rows. Interestingly, the 1/4 ML added row structure is not stable as an intermediate phase between the 1/8 and 1/2 ML added rows, which suggests that there will be a rather abrupt transition between a low coverage of oxygen and the AR- (2×1) reconstruction with 1/2 ML coverage. This could, for instance, become apparent in experiment in the form of AR- (2×1) island formation. As the oxygen exposure further increases to $\Delta\mu_{\text{O}} = -1.46$ eV, the thermodynamic preference changes from the AR- (2×1) to the added strand $c(6 \times 2)$ structure with a 2/3 ML oxygen coverage. The AS- $c(6 \times 2)$ reconstruction is the stable surface phase up to the $\Delta\mu_{\text{O}} = -1.24$ eV bulk-oxide limit. While higher coverage (1 ML) structures were considered by us (see Fig. 8), these do not appear as stable phases in the stability diagram due to the much smaller oxygen binding energies at these coverages. This results in a predicted maximum oxygen coverage of 2/3 ML for the Cu(110) surface. Figure 15 translates these $\Delta\mu_{\text{O}}$ boundaries into a (p, T) phase diagram.

In Fig. 16, the minimum free energy curves of the (100) and (110) crystal faces are combined with the equivalent data for the (111) face (taken from Ref. 57) to predict the oxygen-dependent morphology of copper nanoparticles using Wulff construction.⁷⁹ This procedure determines the nanoparticle shape by balancing within geometrical constraints the relative fractions of the three contributing crystal faces so as to minimize the particles overall surface free energy. These calculations are performed using the program WINXMORPH.^{80,81}

The predicted nanoparticle shapes at four different oxygen chemical potentials are shown in Figs. 16(b)–16(e). Under highly reducing conditions at $\Delta\mu_{\text{O}} = -2.1$ eV, all three crystal faces are free of oxygen, and therefore the shape is deter-

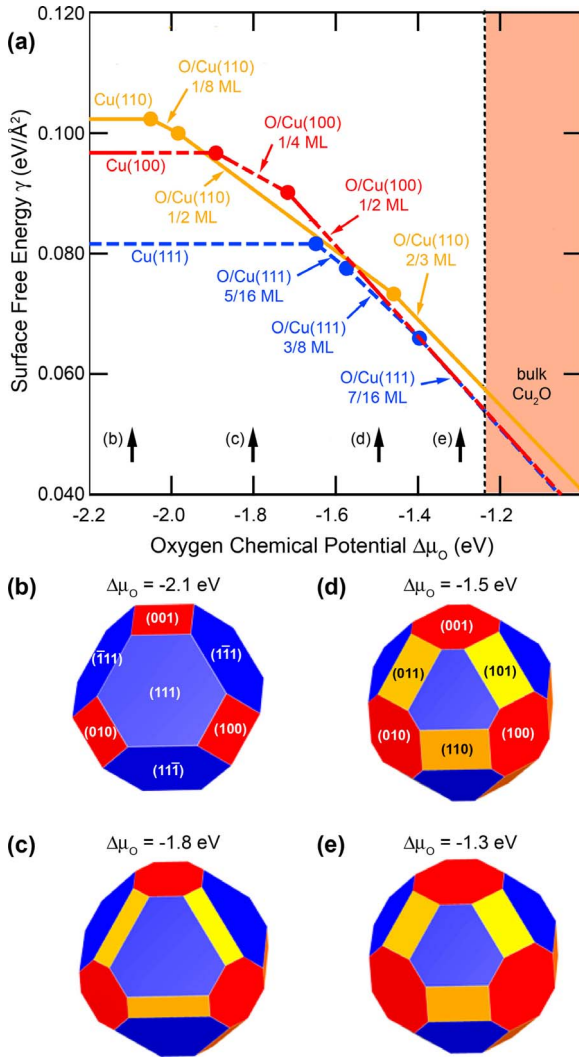


FIG. 16. (Color online) Copper nanoparticle morphology using the Wulff construction. (a) Comparison of the calculated absolute free surface energies γ of (100), (110), and (111) crystal faces as a function of the oxygen chemical potential. (b–d) Predicted nanoparticle shapes for selected values of $\Delta\mu_{\text{O}}$.

mined by the free energies of the clean Cu surfaces. With Cu(111) being considerably more stable than Cu(110) and Cu(100), the nanoparticle shape [Fig. 16(b)] maximizes the exposure of the (111) face; only geometric constraints cause some of the next-favored (100) face to be formed. Figure 16(c) shows the nanoparticle morphology at the higher chemical potential of $\Delta\mu_{\text{O}} = -1.8$ eV at which both the (100) and (110) faces are oxidized, while the (111) remains oxygen free. Oxidation reduces the free energies of the (100) and (110) surfaces, and at $\Delta\mu_{\text{O}} = -1.8$ eV, the (110) face is now slightly more stable than the (100). This change in order manifests itself in the appearance of (110) edges in the nanoparticle shape [Fig. 16(c)]. At $\Delta\mu_{\text{O}} = -1.5$ eV, all three surfaces are oxidized and their free energies are very similar. As a result, all three crystal faces are prominently expressed in

the corresponding particle shape shown in Fig. 16(d)]. Lastly, at $\Delta\mu_{\text{O}} = -1.3$ eV, just prior to bulk oxidation, the free energies of the (111) and (100) surfaces are very nearly degenerate, whereas the (110) is slightly set apart. This results in a slight reduction in the (110) surface area in predicted nanoparticle shape [Fig. 16(e)] relative to the $\Delta\mu_{\text{O}} = -1.5$ eV particle in [Fig. 16(d)].

Overall, the particle shape in the course of oxidation transitions from highly faceted configuration [Fig. 16(b)] to an almost spherical shape [Fig. 16(e)]. This observation can be attributed to the fact that the calculated surface free energies in the absence of oxygen are much more anisotropic than those at the oxygen-rich limit as shown in Fig. 16(a)]. For the latter case, the free energy curves are almost degenerate and, moreover, very nearly parallel. The parallel slope indicates that all three faces, despite differing monolayer coverages, share very similar surface densities of oxygen atoms (between 0.071 and 0.076 atoms/Å² using our GGA unit cell dimensions). The near-degeneracy in the energy in turn suggests that surface free energies at this point are more determined by the mutual proximity of oxygen atoms than by the orientation of the surface.

V. SUMMARY AND CONCLUSIONS

In summary, we have investigated the chemisorption of O on the Cu(100) and Cu(110) surfaces using density-functional theory for a wide range of atomic configurations and coverages, including oxygen adsorbed on ideal and reconstructed surfaces. For the Cu(100) system, oxygen adsorption prefers the hollow site at low oxygen exposures. At higher exposures, the $(2\sqrt{2} \times \sqrt{2})R45^\circ$ missing-row reconstructed structure becomes energetically favored. For the O/Cu(110) system, the [001] Cu-O added row reconstructions are favored at low oxygen exposures, with the AR-(2 × 1) reconstruction prominent under these conditions. At higher oxygen exposures, a transition from the AR-(2 × 1) structure to the $c(6 \times 2)$ added Cu₅O₄-strand structure is predicted to occur. On both crystal faces considered, oxygenated surface structures are stable under conditions prior to onset of bulk oxide Cu₂O formation. Overall, the computational results are broadly consistent with experimental observation, which highlights the ability of DFT free energy calculations to describe the thermodynamics of surface reconstruction for this technologically important material. The combined oxygen-dependent free energies of the (100), (110), and (111) surfaces are used to predict the shape of copper nanoparticles in contact with an oxygen environment.

ACKNOWLEDGMENTS

This research is supported by the Australian Research Council (Grant No. DP0770631), the Australian Partnership for Advanced Computing (APAC), and the Australian Centre for Advanced Computing and Communications (ac3).

- *Present address: Department of Physics, Ningbo University, Ningbo 315211, China.
- †o.warschkow@physics.usyd.edu.au
- ¹A. Guerrero-Ruiz, L. Rodriguez-Ramos, and J. L. G. Fierro, *Appl. Catal.* **72**, 119 (1991).
 - ²G. Centi and S. Perathoner, *Appl. Catal.* **132**, 179 (1995).
 - ³P. J. Godowski, J. Onsgaard, A. Gagor, M. Kondys, and Z. S. Li, *Chem. Phys. Lett.* **406**, 441 (2005).
 - ⁴M. Brandhorst, J. Zajac, D. J. Jones, J. Rozière, M. Womes, A. Jimenez-López, and E. Rodriguez-Castellón, *Appl. Catal., B* **55**, 267 (2005).
 - ⁵I. Louis-Rose, C. Méthivier, and C.-M. Pradier, *Catal. Today* **85**, 267 (2003).
 - ⁶R. W. Mayer, M. Hävecker, A. Knop-Gericke, and R. Schlögl, *Catal. Lett.* **74**, 115 (2001).
 - ⁷C. Fukuhara, H. Ohkura, Y. Kamata, Y. Murakami, and A. Igarashi, *Appl. Catal., A* **273**, 125 (2004).
 - ⁸A. Atkinson, S. Barnett, R. J. Gorte, J. T. S. Irvine, A. J. McEvoy, M. Mogensen, S. C. Singhal, and J. Vohs, *Nature Mater.* **3**, 17 (2004).
 - ⁹F. Luck, *Catal. Today* **27**, 195 (1996).
 - ¹⁰C. Stampfl, M. V. Ganduglia-Pirovano, K. Reuter, and M. Scheffler, *Surf. Sci.* **500**, 368 (2002).
 - ¹¹C. Stampfl, *Catal. Today* **105**, 17 (2005).
 - ¹²M. Wuttig, R. Franchy, and H. Ibach, *Surf. Sci.* **213**, 103 (1989).
 - ¹³H. C. Zeng, R. A. MacFarlane, and K. A. R. Mitchell, *Surf. Sci.* **208**, L7 (1989).
 - ¹⁴M. Wuttig, R. Franchy, and H. Ibach, *Surf. Sci.* **224**, L979 (1989).
 - ¹⁵K. W. Jacobsen and J. K. Nørskov, *Phys. Rev. Lett.* **65**, 1788 (1990).
 - ¹⁶F. Jensen, F. Besenbacher, E. Lægsgaard, and I. Stensgaard, *Phys. Rev. B* **42**, 9206 (1990).
 - ¹⁷I. K. Robinson, E. Vlieg, and S. Ferrer, *Phys. Rev. B* **42**, 6954 (1990).
 - ¹⁸E. A. Colbourn and J. E. Inglesfield, *Phys. Rev. Lett.* **66**, 2006 (1991).
 - ¹⁹M. Sotro, *Surf. Sci.* **260**, 235 (1992).
 - ²⁰F. Besenbacher and J. K. Nørskov, *Prog. Surf. Sci.* **44**, 5 (1993).
 - ²¹T. Lederer, D. Arvanitis, G. Comelli, L. Tröger, and K. Baberschke, *Phys. Rev. B* **48**, 15390 (1993).
 - ²²W. Liu, K. C. Wong, H. C. Zeng, and K. A. R. Mitchell, *Prog. Surf. Sci.* **50**, 247 (1995).
 - ²³T. Fujita, Y. Okawa, Y. Matsumoto, and K.-I. Tanaka, *Phys. Rev. B* **54**, 2167 (1996).
 - ²⁴M. Kittel, M. Polcik, R. Terborg, J. T. Hoeft, P. Baumgärtel, A. M. Bradshaw, R. L. Toomes, J.-H. Kang, D. P. Woodruff, M. Pascal, C. L. A. Lamont, and E. Rotenberg, *Surf. Sci.* **470**, 311 (2001).
 - ²⁵S. Stolbov and T. S. Rahman, *Phys. Rev. Lett.* **89**, 116101 (2002).
 - ²⁶S. Stolbov, A. Kara, and T. S. Rahman, *Phys. Rev. B* **66**, 245405 (2002).
 - ²⁷I. Merrick, J. E. Inglesfield, and H. Ishida, *Surf. Sci.* **551**, 158 (2004).
 - ²⁸M. Alatalo, S. Jaatinen, P. Salo, and K. Laasonen, *Phys. Rev. B* **70**, 245417 (2004).
 - ²⁹T. Kangas, K. Laasonen, A. Puusti, H. Pitkänen, and M. Alatalo, *Surf. Sci.* **584**, 62 (2005).
 - ³⁰A. Puisto, H. Pitkänen, M. Alatalo, S. Jaatinen, P. Salo, A. S. Foster, T. Kangas, and K. Laasonen, *Catal. Today* **100**, 403 (2005).
 - ³¹N. Bonini, A. Kokalj, A. Dal Corso, S. de Gironcoli, and S. Baroni, *Surf. Sci.* **600**, 5074 (2006).
 - ³²M. J. Harrison, D. P. Woodruff, J. Robinson, D. Sander, W. Pan, and J. Kirschner, *Phys. Rev. B* **74**, 165402 (2006).
 - ³³H. Iddir, D. D. Fong, P. Zapol, P. H. Fuoss, L. A. Curtiss, G.-W. Zhou, and J. A. Eastman, *Phys. Rev. B* **76**, 241404(R) (2007).
 - ³⁴S. Jaatinen, M. Rusanen, and P. Salo, *Surf. Sci.* **601**, 1813 (2007).
 - ³⁵T. Kangas and L. Laasonen, *Surf. Sci.* **602**, 3239 (2008).
 - ³⁶K. Lahtonen, M. Hirsimäki, M. Lampimäki, and M. Valden, *J. Chem. Phys.* **129**, 124703 (2008).
 - ³⁷G. Ertl, *Surf. Sci.* **6**, 208 (1967).
 - ³⁸R. A. DiDio, D. M. Zehner, and E. W. Plummer, *J. Vac. Sci. Technol. A* **2**, 852 (1984).
 - ³⁹F. M. Chua, Y. Kuk, and P. J. Silverman, *Phys. Rev. Lett.* **63**, 386 (1989).
 - ⁴⁰F. Jensen, F. Besenbacher, E. Lægsgaard, and I. Stensgaard, *Phys. Rev. B* **41**, 10233 (1990).
 - ⁴¹D. J. Coulman, J. Wintterlin, R. J. Behm, and G. Ertl, *Phys. Rev. Lett.* **64**, 1761 (1990).
 - ⁴²R. Feidenhans'l, F. Grey, R. L. Johnson, S. G. J. Mochrie, J. Bohr, and M. Nielsen, *Phys. Rev. B* **41**, 5420 (1990).
 - ⁴³S. R. Parkin, H. C. Zeng, M. Y. Zhou, and K. A. R. Mitchell, *Phys. Rev. B* **41**, 5432 (1990).
 - ⁴⁴L. Ruan, F. Besenbacher, I. Stensgaard, and E. Laegsgaard, *Phys. Rev. Lett.* **70**, 4079 (1993).
 - ⁴⁵J. Buisset, H.-P. Rust, E. K. Schweizer, L. Cramer, and A. M. Bradshaw, *Surf. Sci.* **349**, L147 (1996).
 - ⁴⁶F. Frechard and R. A. van Santen, *Surf. Sci.* **407**, 200 (1998).
 - ⁴⁷Y. S. Liem, G. Kresse, and J. H. R. Clarke, *Surf. Sci.* **415**, 194 (1998).
 - ⁴⁸Y. Uehara, T. Matsumoto, and S. Ushioda, *Phys. Rev. B* **66**, 075413 (2002).
 - ⁴⁹K. Bobrov and L. Guillemot, *Phys. Rev. B* **78**, 121408(R) (2008).
 - ⁵⁰R. Feidenhans'l, F. Grey, M. Nielsen, F. Besenbacher, F. Jensen, E. Laegsgaard, I. Stensgaard, K. W. Jacobsen, J. K. Nørskov, and R. L. Johnson, *Phys. Rev. Lett.* **65**, 2027 (1990).
 - ⁵¹R. Feidenhans'l, F. Grey, R. L. Johnson, and M. Nielsen, *Phys. Rev. B* **44**, 1875 (1991).
 - ⁵²G. Dorenbos, M. Breeman, and D. O. Boerma, *Phys. Rev. B* **47**, 1580 (1993).
 - ⁵³L. D. Sun, M. Hohage, and P. Zeppenfeld, *Phys. Rev. B* **69**, 045407 (2004).
 - ⁵⁴L. D. Sun, M. Hohage, R. Denk, and P. Zeppenfeld, *Phys. Rev. B* **76**, 245412 (2007).
 - ⁵⁵W. X. Li, C. Stampfl, and M. Scheffler, *Phys. Rev. B* **68**, 165412 (2003).
 - ⁵⁶K. Reuter, C. Stampfl, and M. Scheffler, *Handbook of Materials Modeling* (Springer, Berlin, 2005), Vol. 1.
 - ⁵⁷A. Soon, M. Todorova, B. Delley, and C. Stampfl, *Phys. Rev. B* **73**, 165424 (2006).
 - ⁵⁸J. P. Perdew, K. Burke, and M. Ernzerhof, *Phys. Rev. Lett.* **77**, 3865 (1996).
 - ⁵⁹B. Delley, *J. Chem. Phys.* **113**, 7756 (2000); **92**, 508 (1990).
 - ⁶⁰C. Kittel, *Introduction of Solid State Physics* (Wiley, New York, 1996).
 - ⁶¹A. Soon, L. Wong, B. Delley, and C. Stampfl, *Phys. Rev. B* **77**,

- 125423 (2008).
- ⁶²B. Hammer, L. B. Hansen, and J. K. Nørskov, *Phys. Rev. B* **59**, 7413 (1999).
- ⁶³K. Huber and G. Herzberg, *Molecular Spectra and Molecular Structure IV: Constants of Diatomic Molecules* (Van Nostrand Rienhold, New York, 1979).
- ⁶⁴P. O. Gartland, S. Berge, and B. J. Slagsvold, *Phys. Rev. Lett.* **28**, 738 (1972).
- ⁶⁵X. M. Tao, M. Q. Tan, X. X. Zhao, W. B. Chen, X. Chen, and X. F. Shang, *Surf. Sci.* **600**, 3419 (2006).
- ⁶⁶H. L. Davis and J. R. Noonan, *Surf. Sci.* **126**, 245 (1983).
- ⁶⁷J. L. F. Da Silva, K. Schroeder, and S. Blügel, *Phys. Rev. B* **69**, 245411 (2004).
- ⁶⁸R. Mayer, C. S. Zhang, K. G. Lynn, W. E. Frieze, F. Jona, and P. M. Marcus, *Phys. Rev. B* **35**, 3102 (1987).
- ⁶⁹J. Wan, Y. L. Fan, D. W. Gong, S. G. Chen, and X. Q. Fan, *Modell. Simul. Mater. Sci. Eng.* **7**, 189 (1999).
- ⁷⁰H. P. Bonzel and M. Nowicki, *Phys. Rev. B* **70**, 245430 (2004).
- ⁷¹H. L. Skriver and N. M. Rosengaard, *Phys. Rev. B* **46**, 7157 (1992).
- ⁷²J. L. F. Da Silva, C. Stampfl, and M. Scheffler, *Surf. Sci.* **600**, 703 (2006).
- ⁷³J. L. F. Da Silva, C. Barreateau, K. Schroeder, and S. Blügel, *Phys. Rev. B* **73**, 125402 (2006).
- ⁷⁴G. Cipriani, D. Loffreda, A. D. Corso, S. De Gironcoli, and S. Baroni, *Surf. Sci.* **501**, 182 (2002).
- ⁷⁵M. Gajdoš, A. Eichler, and J. Hafner, *Surf. Sci.* **531**, 272 (2003).
- ⁷⁶C. Stampfl, S. Schwegmann, H. Over, M. Scheffler, and G. Ertl, *Phys. Rev. Lett.* **77**, 3371 (1996).
- ⁷⁷I. Costina, M. Schmid, H. Schiechl, M. Gajdoš, A. Stierle, S. Kumaragurubaran, J. Hafner, H. Dosch, and P. Varga, *Surf. Sci.* **600**, 617 (2006).
- ⁷⁸M. Methfessel, D. Hennig, and M. Scheffler, *Phys. Rev. B* **46**, 4816 (1992).
- ⁷⁹G. Wulff, *Z. Kristallogr. Mineral.* **34**, 449 (1901).
- ⁸⁰W. Kaminsky, *J. Appl. Crystallogr.* **38**, 566 (2005).
- ⁸¹W. Kaminsky, *J. Appl. Crystallogr.* **40**, 382 (2007).